Research Square

Preprints are preliminary reports that have not undergone peer review.
They should not be considered conclusive, used to inform clinical practice,
or referenced by the media as validated information.

Explainable timber geographic provenance using flame emission spectroscopy dynamics and a Transformer model

José I. Cifuentes
University of Concepción
Cristopher Oñate
University of Concepción
Matías Espinoza
University of Concepción
Hugo Garcés
University of Concepción
Nikolaos Salaris
University College London
Rosario Castillo
University of Concepción
Fernando Castillo
fercastillo@udec.cl
University of Concepción

Research Article

Keywords: wood tracing, forestry, spectroscopy, explainable artificial intelligence, deep learning

Posted Date: April 14th, 2026

DOI: https://doi.org/10.21203/rs.3.rs-9047305/v1

License: This work is licensed under a Creative Commons Attribution 4.0 International License.
Read Full License

Additional Declarations: No competing interests reported.

Explainable timber geographic provenance using flame emission spectroscopy dynamics and a Transformer model

José I. Cifuentes[1], Cristopher Oñate[1], Matías Espinoza[1], Hugo Garcés[3], Nikolaos Salaris[4], Rosario Castillo[5], Fernando Castillo[1*]

[1*]Departamento de Ingeniería Eléctrica, Universidad de Concepción, Edmundo Larenas 219, Concepcion, Chile.
[2]Department of Earth, Oceans and Atmospheric Sciences, University of British Columbia, Vancouver, BC, Canada.
[3]Departamento Ingeniería Informática y Ciencias de la Computación, Universidad de Concepción, Concepción, 4070386, Chile.
[4]Department of Mechanical Engineering, University College London, London, WC1E 7JE, United Kingdom.
[5]Departamento de Análisis Instrumental, Facultad de Farmacia, Universidad de Concepción, Concepción, 4070386, Chile.

*Corresponding author(s). E-mail(s): fercastillo@udec.cl;
Contributing authors: jcifuentes@eoas.ubc.ca; cconate2018@udec.cl; matiasaespinoza@udec.cl; hugarces@udec.cl; n.salaris@ucl.ac.uk; rosariocastillo@udec.cl;

Abstract

The misrepresentation of timber provenance undermines global supply chain transparency and sustainable forest management practices. Although reference forensic approaches, such as stable isotope analysis and chemical and genetic approximations, are reliable, their high cost and complexity hinder their widespread adoption. This work evaluates the feasibility of a high-throughput framework for provenance classification that integrates VIS-NIR flame emission spectroscopy dynamics and an end-to-end deep learning model. *Eucalyptus globulus* samples were harvested from five distinct geographical sectors in Chile and subjected to controlled combustion. Combustion kinetic profiles were recorded

using a VIS-NIR spectrophotometer and processed using Transformer architecture, benchmarked against Support Vector Machine (SVM) and XGBoost classifiers. The proposed model achieved a test accuracy and F1-score of 97.5%, significantly outperforming SVM (80.0%) and XGBoost (62.5%) baselines. Traditional models exhibited severe overfitting owing to static feature compression, whereas the Transformer successfully captured the transient temporal patterns of the combustion cycle. Interpretable feature attribution analysis using Shapley Additive exPlanations (SHAP) confirms that the classification relies on specific atomic emission lines (potassium doublet at 766.4 and 770.1 nm), validating the physico-chemical basis of the model. These findings confirm that treating wood provenance as a dynamic pattern recognition task yields superior robustness, providing a data-efficient basis for a compact optical sensor for traceability that complements existing timber tracing frameworks.

Keywords: wood tracing, forestry, spectroscopy, explainable artificial intelligence, deep learning

1 Introduction

Timber authentication and provenance verification increasingly require analytical methods that are rapid, objective, and scalable for routine screening at checkpoints, mills, and borders [1]. Wood is a strategic and widely used material across sectors such as construction, manufacturing, design, energy, and heating, with a global supply chain [2–4]. However, this supply chain faces persistent challenges in terms of illegal logging. Worldwide, the associated economic losses are estimated at US$30–100 billion per year, and in some countries, illegally sourced timber may account for up to 90% of sector exports [5]. In the Amazon, losses have been reported in the order of US$558–639 million, while in Chile estimates are around US$200 million [6, 7]. In addition to the economic and social impacts caused by market distortion, tax evasion, and unfair competition, illegal logging threatens protected species, degrades habitats, and undermines key ecosystem services [8, 9].

In response, substantial international, regulatory, and market-based efforts have been made to curb illegal logging by tightening enforcement, mandating due diligence, and expanding certification and traceability schemes [10, 11]. However, a persistent bottleneck across these initiatives is the ability to quickly and reliably verify timber provenance in operational settings, which is essential for preventing the entry of illegally harvested wood into legitimate supply chains [1]. Currently, prevailing forensic approaches, such as genetic approximations and chemical or isotopic fingerprinting, have major drawbacks: they typically require specialist laboratories and considerable time and cost [12–14]. While these methods remain reference benchmarks for wood provenance studies, their analytical complexity and high operational costs often restrict large-scale adoption [15, 16].

Spectroscopic techniques have been increasingly established for discriminating wood species and their geographic origins. Visible-near-infrared (VIS–NIR) spectroscopy can be used to characterize wood and its derivatives by identifying the

physicochemical signatures encoded during their growth [17–19]. Notable studies have demonstrated the efficacy of coupling reflectance data with chemometrics to identify timber provenance under controlled conditions, establishing these methods as robust tools for laboratory-based screening [20–22]. Although the broader literature supports these workflows, significant operational constraints remain. Sensitivity to moisture content, surface roughness, and instrument calibration needs hinder cross-site deployment, highlighting the need for more robust verification systems and robust chemometric techniques [23–26].

Although VIS–NIR reflectance spectroscopy of solid samples remains the standard for wood identification, recent studies have highlighted that chemical signatures can also be extracted from visible flame emission spectra [27]. When coupled with supervised machine learning, temporal-spectral features in the 450–900 nm range, such as the K/Na ratio, flame temperature, and total continuous radiation, have been shown to encode sufficient physico-chemical information for robust discrimination. This positions flame emission spectroscopy as a rapid, cost-effective complement to conventional reflectance methods, with the potential to probe elemental composition linked to growth conditions.

In Chile, *Eucalyptus globulus* is a strategically relevant hardwood for industrial forestry, particularly because of its importance in timber and pulp-related value chains [28]. From an analytical standpoint, provenance verification is non-trivial because growth conditions can modulate the physicochemical properties that ultimately influence the optical signatures measured either in reflectance or in combustion emission [25, 29]. This makes *Eucalyptus globulus* a suitable and practically motivated target species for evaluating provenance classification methods that aim to operate under scalable screening paradigms in the future.

This study applies visible-near-infrared (VIS–NIR) combustion spectroscopy (450–850nm) to determine the provenance of *Eucalyptus globulus* using samples collected from five distinct sectors in the Bio-Bío Region of south-central Chile [28]. We aim to show that spectral variations in the emission profile reflect distinct site-related chemistry, thereby enabling geographic classification. Unlike traditional approaches that reduce the burning event to average values, this study treats each sample as a kinetic physico-chemical process. By analyzing the full temporal patterns of the emission lines, we aim to extract transient provenance signatures that are otherwise lost in static aggregation.

We applied chemometric techniques to correlate spectral emission dynamics with geographical provenance, benchmarking the proposed Transformer network against Support Vector Machine (SVM) and Extreme Gradient Boosting (XGBoost) baselines. The models were trained using input vectors that combined broadband emission profiles with discrete line intensities. Cross-validation was used to assess the generalization performance across the harvest sectors. This work validates the feasibility of a rapid and cost-effective provenance classification framework. By combining flame emission spectroscopy with deep learning, this framework offers a robust tool for verifying the origin of *Eucalyptus globulus*, providing a potentially scalable solution for combating illegal logging and strengthening supply chain integrity.

The contributions of this work are enumerated as follows:

1. Development of a high-throughput framework integrating visible-range flame-emission spectroscopy dynamics with deep learning, establishing a basis for a compact optical sensor for rapid and cost-effective timber provenance verification.
2. Utilization of multivariate combustion kinetics as the primary input to capture the dynamic evolution of combustion and its inherent physico-chemical signatures, preserving transient information that is lost in static feature engineering methods that compress data into global statistics.
3. Proposal of an end-to-end trainable Transformer pipeline optimized for spectral time-series, which captures temporal dependencies effectively, improving generalization compared to classical baselines such as SVM and XGBoost.
4. Validation of spectral fingerprint consistency via SHAP analysis, confirming that predictions are driven mainly by atomic emissions (K).

The article is organized as follows: Section 2 provides fundamental aspects of flame emission spectroscopy. Section 3 details the experimental workflow, ranging from sample acquisition and spectral preprocessing to the implementation of the Transformer architecture and explainable artificial intelligence (XAI). Section 4 analyzes the classification performance and discusses the interpretability of the results. Finally, Section 5 summarizes the main conclusions.

2 Fundamentals of Combustion Spectroscopy

2.1 Spectral theory of the flame

Across the spectral ranges reported for biomass combustion, flame emission spectra are typically characterized by a smooth broadband continuum alongside discontinuous spectral features [30, 31]. The broadband continuum is usually linked to radiation from incandescent particulates (e.g., soot), whereas the discrete bands and lines arise from the spontaneous emission of excited radicals, molecules, and atomic species. Fig. 1 shows a representative spectrum in which the continuum and atomic signatures appear simultaneously. Because biomass can retain inorganic constituents, alkali emissions are commonly observed during burning; in particular, Na near 589.4 nm and K near 766.4 and 770.1 nm are often among the most prominent atomic features [32]. Combustion spectra are also frequently interpreted in relation to blackbody radiation, which motivates emissivity-based descriptions to capture the departures from ideal thermal behavior [33, 34].

Flame emission is inherently geometry dependent. The radiating flame volume is emitted into the full solid angle with a spatial distribution that is generally non-isotropic [35]. As a result, the recorded spectrum depends on the collection optics, line of sight, and effective field of view and should be interpreted alongside instrumental effects. The relevant sources of uncertainty include stray light, deviations from an ideal cosine response, and detector dark signals, all of which can bias the continuum level and distort the apparent strength of discrete features [36, 37]. Accordingly, the measured emission spectrum E_m can be modeled as the sum of a continuous component $E_c(\lambda, t)$, discrete-line component $E_d(\lambda, t)$, and additive noise term $n(t)$:

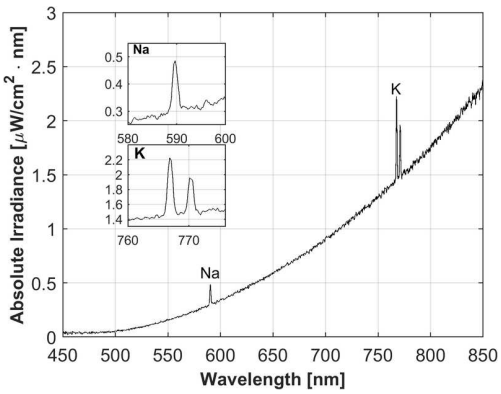


Fig. 1 Emission spectra during the combustion of *Eucalyptus globulus*.

$$E_m(\lambda, t) = E_c(\lambda, t) + E_d(\lambda, t) + n(t) \tag{1}$$

where λ denotes the wavelength and t is the discrete time. The term $n(t)$ summarizes random fluctuations in the acquisition chain, which are often dominated by the detector dark current in radiometrically calibrated measurements.

3 Material and methods

The experimental framework implemented in this study connects the physical wood properties to geographical provenance through a multistage pipeline, as illustrated in Fig. 2.

3.1 Data collection

The primary dataset comprised trees harvested from five geographically distinct forest sectors in Chile. The specific geodetic coordinates for each sampling site are detailed in Table 1, and their spatial distribution is illustrated in Fig. 3. Wood blocks were prepared from each tree following the standard dimensions described in the subsequent section.

Table 1 Geodetic coordinates, mean mass (± standard deviation), and number of spectra for the five *Eucalyptus globulus* sampling sectors in the Bio-Bío Region, Chile.

Sector	Location	Mass [g]	N° spectra
1	36°56'30"S 72°55'23"W	1.02 ± 0.14	10519
2	36°58'57"S 72°55'22"W	1.05 ± 0.18	12182
3	37°16'34"S 72°41'31"W	1.06 ± 0.10	9673
4	37°15'19"S 72°42'10"W	1.07 ± 0.12	12776
5	37°00'51"S 72°58'17"W	1.01 ± 0.13	10210

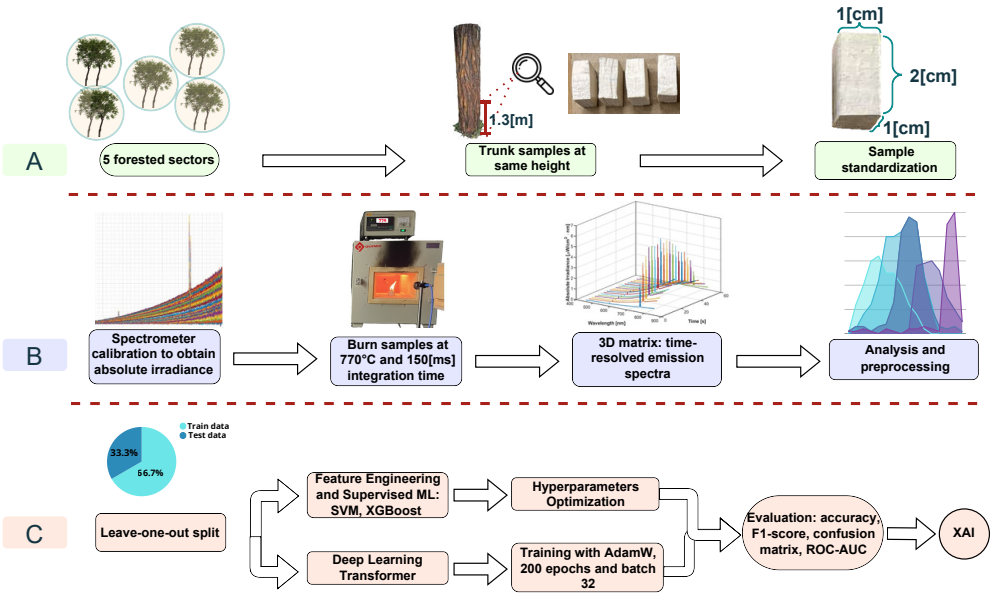


Fig. 2 Summary of the methodological workflow, including **(A)** field sampling and standardization, **(B)** controlled combustion and spectral acquisition, and **(C)** data partitioning, feature extraction, and classification with machine-learning and Transformer models.

The experimental design adopted a standardized sampling height for all trees. Transverse discs of *Eucalyptus globulus* were harvested at 1.3 m above the ground, corresponding to the conventional breast-height (DBH) level commonly used in forest inventory and wood property studies [38]. After removing the bark, a sapwood block of approximately 6×5 cm was extracted. From each sapwood block, one uniform sample ($2 \times 1 \times 1$ cm) was prepared and combusted following the procedure described in Section 3.3. A total of 24 samples were prepared per zone from different trees (120 samples across all zones).

To mitigate spectral interference from moisture absorption bands [39], the samples were dehydrated in an oven at 105 °C for 5 h, according to UNE-EN ISO 18134 [40]. After conditioning, all samples were subjected to the combustion protocol described in Section 3.3.

3.2 Spectral acquisition setup

To conduct the experiments, the setup shown in Fig. 4 was implemented as follows [27]. The combustion was monitored using a calibrated VIS-NIR HR-4000 spectrophotometer (Ocean Insight Inc.) with a spectral resolution of $\Delta\lambda \approx 0.25$ nm and a spectral range from 200 to 1100 nm,together with an optical fiber and a collimating lens to cover the entire solid angle of the flame. Spectral data acquisition was performed with an integration time of 150 ms using a graphical user interface developed in LabView (National Instruments).

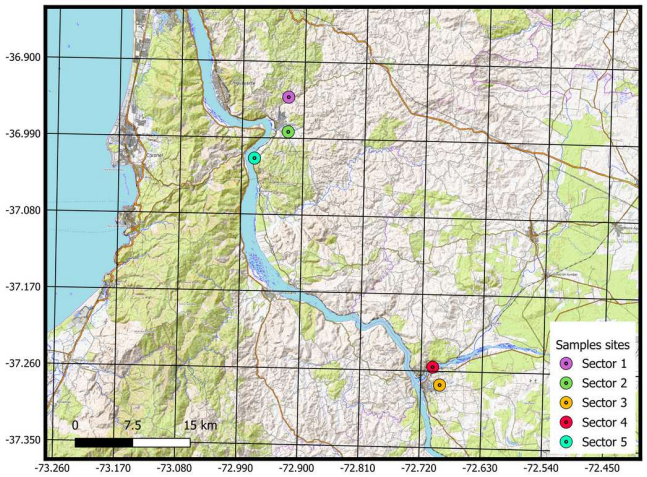


Fig. 3 Geographical distribution of the sampling sites. The map illustrates the spatial arrangement of the five *Eucalyptus globulus* harvesting sectors in the Bio-Bío Region, Chile. Colored markers correspond to the coordinate centroids listed in Table 1.

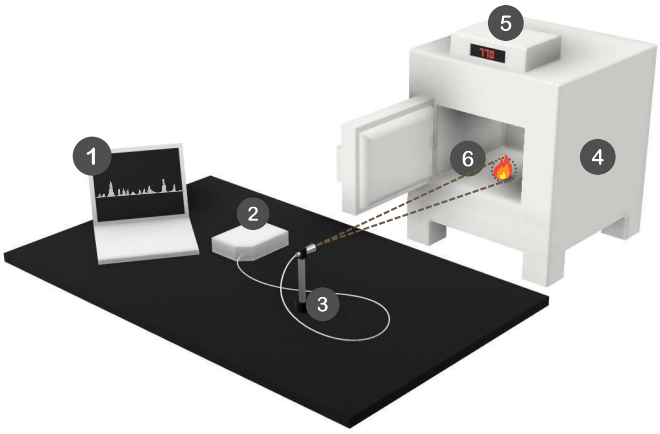


Fig. 4 Schematic of the experimental setup for combustion emission spectroscopy. **(1)** Data acquisition workstation; **(2)** High-resolution spectrometer radiometrically calibrated for absolute irradiance; **(3)** Optical fiber assembly equipped with a collimating lens (dashed line indicates the Field of View); **(4)** Electric muffle furnace; **(5)** PID temperature controller; and **(6)** Wood sample undergoing combustion within the thermal chamber.

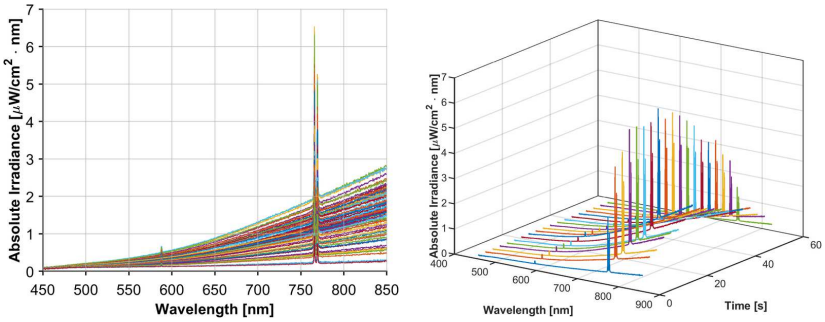
3.3 Combustion protocol

The measurements were conducted following a controlled procedure comprising the following steps:

1. For each sample, the furnace was stabilized at 770 °C and the spectrometer with 150 ms as integration time.
2. Once the furnace reached 770 °C, the wood sample was introduced and placed directly on a ceramic crucible located at the center of the furnace.
3. Spectral acquisition was immediately initiated, recording ignition, the full combustion process, and flame extinction.
4. After flame extinction, the residual sample was carefully removed, and the next sample was introduced. This procedure was repeated until all the samples were completely combusted. Finally, all collected data were stored.

All measurements described in this study were performed according to this procedure. Any modifications to the configuration parameters are explicitly indicated in the respective experimental sections.

In Fig. 5, the final radiometrically calibrated spectra are shown, acquired every 150 ms over the full biomass combustion process, from ignition to flame extinction, using the HL-2000-FHSA lamp for calibration.



(a) (b)

Fig. 5 Visible band emission spectra during a sample *Eucalyptus globulus* combustion: **(a)** 2-D matrix of calibrated spectra across the entire burn; **(b)** 3-D subsampled view every 15th spectrum.

3.4 Dataset formalization and preprocessing

The dataset comprises spectro-kinetic profiles of combustion emissions acquired from *Eucalyptus globulus* specimens across $K = 5$ distinct geographical sectors. Let $S = 120$ denote the total number of observed spectral dynamic processes. Each spectral process $i \in \{1, \ldots, S\}$ is represented by a multivariate sequence $\mathbf{X}_i \in \mathbb{R}^{T_i \times \Lambda}$, where T_i denotes the variable number of temporal frames recorded during combustion, and $\Lambda = 1560$ represents the number of spectral bands (wavelengths). Each process is associated with a label $y_i \in \{1, \ldots, K\}$, corresponding to its geographical origin. The class labels correspond directly to the geographical sectors defined in Table 1.

To handle variable sequence lengths within tensor operations, sequences are zero-padded to a global maximum length $T_{\max} = \max_i T_i$. We define a binary mask matrix $\mathbf{M}_i \in \{0, 1\}^{T_{\max}}$, where $M_{i,t} = 1$ indicates that the t-th frame is a valid measurement from the original sequence and $M_{i,t} = 0$ denotes padding.

3.4.1 Data partitioning

All samples originating from the same tree were assigned exclusively to the training or test set. The dataset was partitioned into a training set $\mathcal{I}_{\text{tr}}$ ($|\mathcal{I}_{\text{tr}}| = 80$) and a test set $\mathcal{I}_{\text{te}}$ ($|\mathcal{I}_{\text{te}}| = 40$). Considering the total of 55360 spectral emission dynamics across all sectors (Table 1), this partition yields approximately 37000 spectra in $\mathcal{I}_{\text{tr}}$ and 18000 spectra in $\mathcal{I}_{\text{te}}$.

3.4.2 Spectral normalization

To ensure spectral comparability and prevent high-intensity emission lines from dominating the loss gradients, the inputs were standardized using Z-score normalization.

Let $\mathcal{T}_{\text{valid}} = \{(i,t) \mid i \in \mathcal{I}_{\text{tr}} \wedge M_{i,t} = 1\}$ denote the set of valid spatiotemporal indices in the training set. By aggregating all time-steps, the normalization statistics were derived from approximately 37000 independent spectral observations. The mean μ_λ and standard deviation σ_λ for each spectral band $\lambda \in \{1, \ldots, \Lambda\}$ are computed as:

$$\mu_\lambda = \frac{1}{|\mathcal{T}_{\text{valid}}|} \sum_{(i,t)\in\mathcal{T}_{\text{valid}}} X_{i,t,\lambda} \tag{2}$$

$$\sigma_\lambda = \sqrt{\frac{1}{|\mathcal{T}_{\text{valid}}|} \sum_{(i,t)\in\mathcal{T}_{\text{valid}}} (X_{i,t,\lambda} - \mu_\lambda)^2 + \epsilon} \tag{3}$$

where ϵ is a small constant (10^{-5}) for numerical stability. The normalized tensor $\tilde{\mathbf{X}}$ is then obtained element-wise, ensuring that the padded values remain zero:

$$\tilde{X}_{i,t,\lambda} = \frac{X_{i,t,\lambda} - \mu_\lambda}{\sigma_\lambda} \cdot M_{i,t} \tag{4}$$

3.4.3 Feature engineering

For the classical machine learning baselines (SVM and XGBoost), the temporal dimension was collapsed via statistical aggregation. We computed the mean and standard deviation across the time axis for each spectral band, resulting in a static tabular representation $\mathbf{Z}_i \in \mathbb{R}^{2\Lambda}$, where the feature dimension is $2\Lambda = 3120$.

3.5 Model framework and hyperparameter optimization

We employed Support Vector Machine (SVM) and Extreme Gradient Boosting (XGBoost) as baseline classifiers. The hyperparameters were optimized via a grid search with stratified 5-fold cross-validation, selecting the configuration that maximized the validation accuracy. The search space was defined as follows:

1. For the XGBoost implementation, we used the Python library `xgboost`, configured with the histogram-based tree construction method. The model employs a multi-class softmax objective with 300 estimators. The grid search explores the following parameters: maximum tree depth $\{6, 11\}$, learning rate $\{0.1, 0.05\}$, subsample ratio $\{0.8\}$, column sampling ratio per tree $\{0.8, 1.0\}$, L_1 regularization

$\lambda_1 \in \{0, 0.1, 1.0\}$, L_2 regularization $\lambda_2 \in \{0.1, 1.0\}$, booster type {`dart`, `gbtree`}, dropout rate $\{0.15, 0.25\}$, and drop probability $\{0, 0.15\}$.

2. The SVM was trained using a linear kernel implemented via the `libsvm` backend with the penalty parameter $C \in \{10^3, 10^2, \ldots, 10^{-3}\}$.

3.6 Transformer spectral classification framework

To capture long-range temporal dependency patterns in the combustion emission spectra, we propose a Transformer architecture (Fig. 6). The model input consists of a normalized time spectral tensor $\mathbf{X} \in \mathbb{R}^{T \times \Lambda}$, where T represents the temporal sequence length corresponding to the burning process (padded to $T_{\max}$), and $\Lambda = 1560$ denotes the number of spectral bands.

3.6.1 Architecture framework

The input sequence $\mathbf{X}$ is projected using a learnable linear transformation. To maintain the sequential order of the spectral frames, learnable positional embeddings are incorporated into the transformed input [41]. Let $\mathbf{H}^{(l)} \in \mathbb{R}^{T \times d_{\text{model}}}$ denote the output of the l-th layer:

$$\mathbf{H}^{(0)} = \text{Linear}(\mathbf{X}) + \mathbf{PE}(T), \tag{5}$$

where $\text{Linear}(\mathbf{X}) \in \mathbb{R}^{T \times d_{\text{model}}}$ and $\mathbf{PE} \in \mathbb{R}^{T \times d_{\text{model}}}$.

The architecture comprises L Transformer encoder blocks for any layer $l \in \{0, \ldots, L-1\}$. To compute the output $\mathbf{H}^{(l+1)}$, the MHA mechanism first projects each input $\mathbf{H}^{(l)}$ into query ($\mathbf{Q}$), key ($\mathbf{K}$), and value ($\mathbf{V}$) matrices. The attention scores for a specific head i are computed as follows:

$$\text{head}_i = \text{Softmax}\left(\frac{\mathbf{Q}_i \mathbf{K}_i^\top}{\sqrt{d_k}}\right)\mathbf{V}_i \tag{6}$$

where $\mathbf{Q}_i = \mathbf{H}^{(l)}\mathbf{W}_i^Q$, $\mathbf{K}_i = \mathbf{H}^{(l)}\mathbf{W}_i^K$, and $\mathbf{V}_i = \mathbf{H}^{(l)}\mathbf{W}_i^V$ are obtained via learned projections $\mathbf{W}_i^{\{Q,K,V\}} \in \mathbb{R}^{d_{\text{model}} \times d_k}$, with $d_k = d_{\text{model}}/h$. The heads are then concatenated and projected linearly:

$$\text{MHA}(\mathbf{H}^{(l)}) = \text{Concat}(\text{head}_1, \ldots, \text{head}_h)\mathbf{W}^O \tag{7}$$

where $\mathbf{W}^O \in \mathbb{R}^{d_{\text{model}} \times d_{\text{model}}}$. The output is then normalized:

$$\mathbf{Z}^{(l)} = \mathcal{LN}\left(\mathbf{H}^{(l)} + \text{MHA}(\mathbf{H}^{(l)})\right). \tag{8}$$

Then, the position-wise FFN processes the sequence using a Gaussian Error Linear Unit (GeLU) activation [42]:

$$\text{FFN}(\mathbf{Z}^{(l)}) = \text{GeLU}(\mathbf{Z}^{(l)}\mathbf{W}_1 + \mathbf{b}_1)\mathbf{W}_2 + \mathbf{b}_2, \tag{9}$$

then, the output of the layer is obtained as follows:

$$\mathbf{H}^{(l+1)} = \mathcal{LN}\left(\mathbf{Z}^{(l)} + \text{FFN}(\mathbf{Z}^{(l)})\right). \tag{10}$$

Finally, the output sequence of the last encoder block, $\mathbf{H}^{(L)}$, is pooled and projected into a feature space $\mathbf{f} \in \mathbb{R}^{d_{\text{model}}}$.

3.6.2 Transformer hyperparameters and simulation specifications

The model was instantiated with a latent dimensionality of $d_{\text{model}} = 128$. The input stage incorporates a dense projection and learnable positional encoding to preserve the temporal order. The encoder consists of $L = 2$ stacked Transformer blocks, employing MHA with $h = 4$ heads and a head dimension of $d_k = d_{\text{model}}/h = 32$ (Fig.6). Following feature extraction, the temporal dimension is aggregated via Global Average Pooling to generate a fixed-length context vector. This representation is fed into a classification head comprising a dense layer (128 units, Dropout $p = 0.3$) and a final Softmax output layer corresponding to the $K = 5$ provenance sectors.

The model was implemented in PyTorch and trained on an NVIDIA A100 GPU (40 GB VRAM) and 128 GB of system RAM. Optimization was performed using the AdamW algorithm [43] with a learning rate of 1×10^{-4} and a reduction factor $\gamma = 0.75$ every 25 epochs. Training was performed using a batch size of 32 for 200 epochs with stratified shuffle sampling.

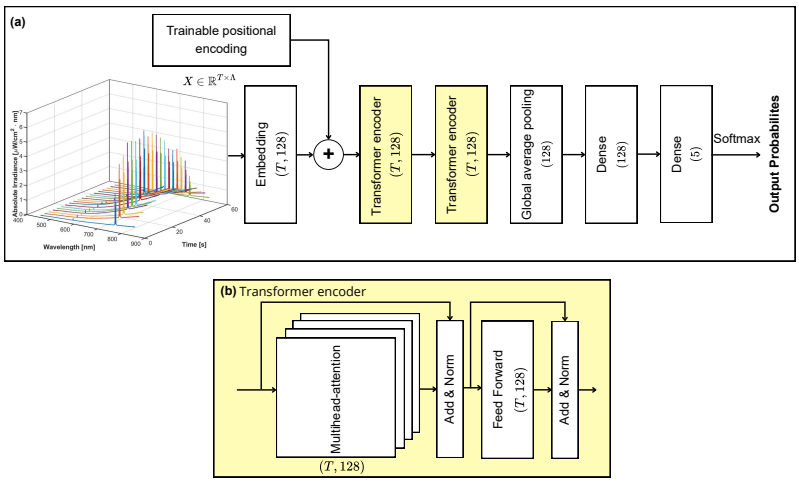


Fig. 6 Schematic of the proposed deep learning architecture. **(a)** The spectral time-series tensor $\mathbf{X}$ is embedded, processed by two Transformer blocks, and pooled for classification. **(b)** Transformer encoder block composed by the Multi-head attention and feed-forward sublayers with residual connections.

3.7 Evaluation metrics

For K-class classification problem, let C_{ij} denote the element of the confusion matrix corresponding to samples of true class i predicted as class j. Furthermore, the true positives ($\text{TP}_i = C_{ii}$), true negatives ($\text{TN}_i = \sum_{\substack{j \neq i \\ k \neq i}} C_{jk}$), false positives ($\text{FP}_i = \sum_{j \neq i} C_{ji}$), and false negatives ($\text{FN}_i = \sum_{j \neq i} C_{ij}$) are defined. Finally, the overall accuracy (Acc) and macro-averaged F_1-score were computed as in Eqs: 11 and 12, respectively.

$$\text{Acc} = \frac{1}{S} \sum_{i=0}^{K-1} C_{ii} \tag{11}$$

$$F_1 = 2 \cdot \frac{\text{Precision} \cdot \text{Recall}}{\text{Precision} + \text{Recall}} \tag{12}$$

where,

$$\text{Precision}_i = \frac{\text{TP}_i}{\text{TP}_i + \text{FP}_i}, \quad \text{Recall}_i = \frac{\text{TP}_i}{\text{TP}_i + \text{FN}_i} \tag{13}$$

Furthermore, we employed Receiver Operating Characteristic (ROC) and area Under the Curve (AUC) (Eq.(15)) metrics to convey the model performance. To generate ROC curves, we illustrated the True Positive Rate (TPR) against the False Positive Rate (FPR). The TPR and FPR are defined as follows:

$$\text{TPR}_i = \frac{\text{TP}_i}{\text{TP}_i + \text{FN}_i}, \quad \text{FPR}_i = \frac{\text{FP}_i}{\text{FP}_i + \text{TN}_i} \tag{14}$$

$$\text{AUC} = \int_0^1 \text{TPR}(\text{FPR})\, \text{d}(\text{FPR}) \tag{15}$$

3.8 Explainable artificial intelligence (XAI)

We utilized SHapley Additive exPlanations (SHAP) to confirm the geochemical consistency of the model predictions [44, 45]. SHAP enables us to determine the individual impact of each spectral feature on the model output. In the context of flame emission spectroscopy, the SHAP value ϕ_i represents a specific wavelength intensity feature i is calculated as follows:

$$\phi_i(f, x) = \sum_{S \subseteq \mathcal{M} \setminus \{i\}} \frac{|S|!(|\mathcal{M}| - |S| - 1)!}{|\mathcal{M}|!} \left[f_x(S \cup \{i\}) - f_x(S) \right] \tag{16}$$

where f_x is the model prediction function, $\mathcal{M}$ are he input features, and $|\mathcal{M}|$ denotes the total count of these features. S represents a subset of features excluding i ($S \subseteq \mathcal{M} \setminus \{i\}$), and $f_x(S)$ denotes the expected prediction conditioned on the feature subset S.

4 Results and Discussion

4.1 Comparative benchmarking and generalization capability

Table 2 highlights the generalization capabilities of each odel. While all architectures achieved high training accuracy ($\geq$ 93%), a critical analysis of the training-to-test gap exposed the limitations of static feature engineering. The XGBoost classifier exhibited severe overfitting, collapsing from 93.85% (train) to 62.5% (test). This degradation indicates that the gradient boosting ensemble likely memorized high-frequency

noise specific to the training sectors and failed to capture the invariant geochemical signature, similarly, the SVM baseline showed a decline (80.0% test accuracy).

Table 2 Mean performance benchmarking of classification models on the time series spectral dataset.

Model	Accuracy		F1-Score	
	Train	Test	Train	Test
XGBoost	93.85% ± 3.95%	62.5%	93.77% ± 4.03%	61.9%
SVM	93.75% ± 5.30%	80.0%	93.46% ± 5.49%	73.3%
Transformer	**96.25% ± 4.76%**	**97.5%**	**95.38% ± 3.59%**	**97.5%**

In contrast, the Transformer architecture demonstrated superior robustness, achieving a test accuracy of 97.5%. The test performance slightly surpasses the mean training accuracy (96.25%). This behavior is consistent with the use of regularization, which suppresses the model capacity during training to force the learning of redundant, robust features, whereas the full network capacity is utilized during inference. As shown in the confusion matrices (Fig. 7), the transformer effectively resolves the class confusion (specifically between Classes 1 and 3) that confounded the baselines.

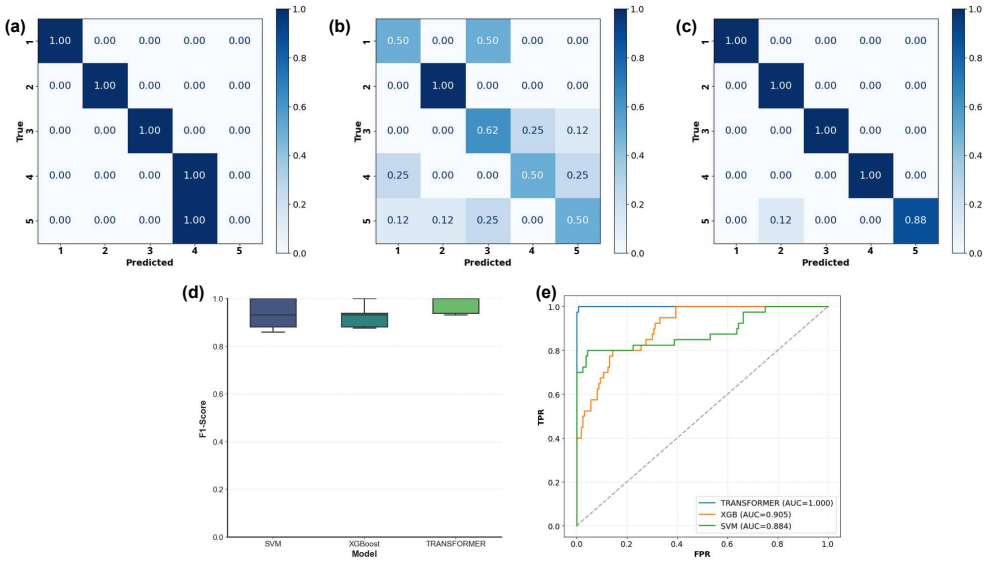


Fig. 7 **(a)-(c)** Normalized confusion matrices for the classification models using the test data **(a)** SVM, **(b)** XGBoost, **(c)** Transformer. **(d)** F1-score 5-fold cross validation results **(e)** ROC curve comparing the performance of the three models with AUC value for each model.

The performance can be explained by examining the attention profiles (Fig. 8d). The MHA acts as a dynamic regularizer, consistently prioritizing the potassium emission doublet ($\sim 766.4, 770.1\,\text{nm}$) and suppressing stochastic continuum spectra. This allows the model to effectively optimize the bias-variance trade-off, even with a limited number of replicates.

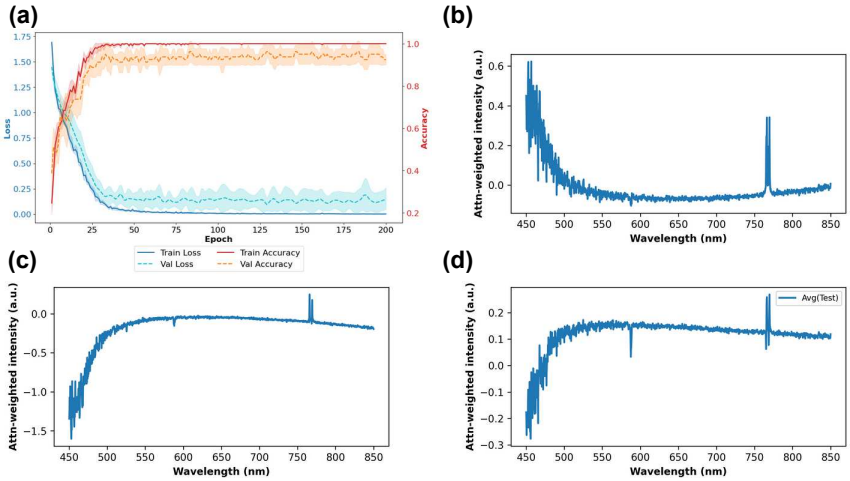


Fig. 8 Transformer training dynamics and attention mechanism analysis. **(a)** Evolution of Cross-Entropy Loss and Accuracy over 200 epochs (mean and standard deviation). **(b)–(c)** Attention-weighted spectral profiles (computed via Eq.6) for representative samples from Class 3 and Class 1, respectively. **(d)** Global average attention profile across the test set.

Although the number of independent samples is $N = 120$, the Transformer operates on the full spectral–temporal tensor $\mathbf{X} \in \mathbb{R}^{S\times T\times \Lambda}$, exploiting the complete time-resolved emission dynamics rather than a static compression. Classical baselines, such as SVM and XGBoost, depend on hand-crafted, time-aggregated descriptors, which collapse the temporal axis and suppress transient combustion phenomena. In contrast, our acquisition yields an average sequence duration of ≈ 45 s, corresponding to $T \approx 460$ spectral time steps per sample across $\Lambda = 1560$ wavelengths. This temporal resolution enables the model to capture intra-sequence dependencies and alkali release kinetics (e.g., K/Na-related transients) that are not accessible to static classifiers based on global summary statistics.

The temporal variability discarded by averaging constitutes the discriminative signal. By exploiting the temporal structure of the data, the Transformer distinguishes spectral signatures based on their specific occurrence within the combustion dynamics. For instance, two wood samples may exhibit identical mean potassium intensities (indistinguishable from SVM) but distinct release rates (distinguishable from the Transformer). This confirms that in complex physico-chemical processes, the sequence itself carries provenance information embedded within the spectro-kinetic evolution of the sample, which is distinct from its static chemical composition.

4.2 Explainability of spectral combustion dynamics

The performance hierarchy outlined in the previous section, which highlights the instability of clasical machine learning techniques compared to the robustness of the Transformer, can be physically explained by the distinct feature prioritization strategies of each architecture. SHAP analysis reveals a fundamental divergence: while baselines struggle to decouple the signal from noise, the Transformer consistently anchors its predictions on atomic emission.

Figure 9 reveals convergence in feature selection between the SVM and Transformer, particularly regarding the alkali emission lines. Both architectures identified the potassium doublet (766.4, 770.1 nm) as the primary discriminator. The relative success of SVM over XGBoost can be attributed to this geochemical anchoring; by prioritizing the stable Na/K emission ratios, the kernel-based model mitigates the influence of transient spectral artifacts. In contrast, the XGBoost model (Fig. 9c) assigns disproportionate gain to the 451 nm band in isolation. This suggests that the gradient boosting ensemble overfitted to high-frequency noise or secondary combustion byproducts specific to the training partitions, and failed to extract the invariant provenance signal.

However, the Transformer extends beyond the linear dependency modeled by the SVM. As detailed in Fig. 10, while the network retains the potassium signature (766.4, 770.1 nm) as a central anchor, it successfully integrates a secondary region in the blue-violet band (450-460 nm). Unlike the XGBoost baseline, that relies on the 451 nm band as the primary splitting feature; This allows the Transformer model to combine the chemical stability of atomic emission lines with subtle nonlinear variations in the background continuum, achieving robust generalization for unseen samples. This supports the compact optical sensor concept for rapid provenance screening.

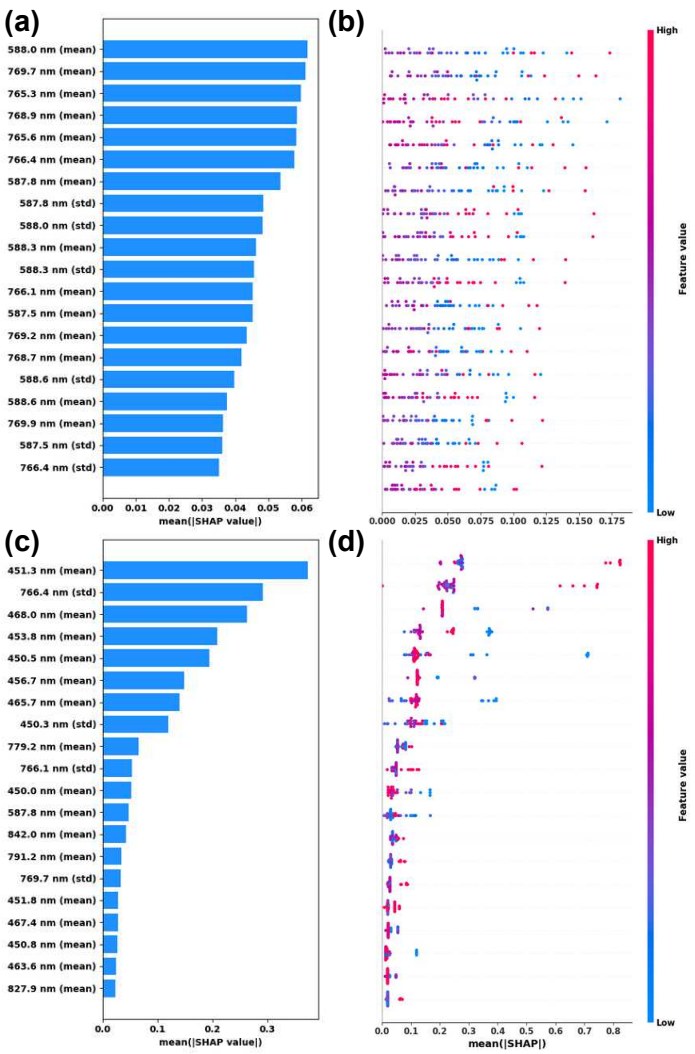


Fig. 9 Global SHAP comparison for baseline classifiers. **(a)** and **(c)** Feature importance rankings for SVM and XGBoost, respectively. Note the SVM model uses on alkali doublets (Na ∼587.8 nm, K ∼ 766.4, 770.1 nm) versus the XGBoost prioritization of the 451 nm band. **(b)** and **(d)** Corresponding beeswarm density plots indicating feature impact directionality.

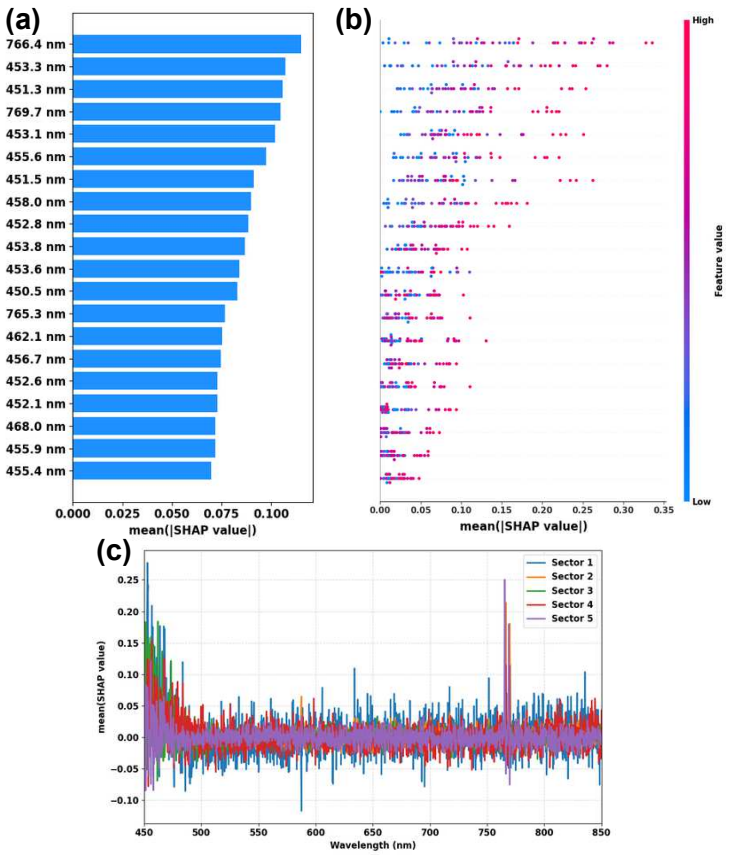


Fig. 10 Transformer interpretability analysis. **(a)** Global feature importance, highlighting the K emission ($\sim 766.4, 770.1$ nm) and the 450–460 nm spectral cluster. **(b)** Beeswarm summary plot. **(c)** Mean SHAP values stratified by provenance sector (1–5), illustrating feature relevance across the spectral sequence.

5 Conclusion

This work proposes and evaluates a novel technique of visible-range flame emission spectroscopy (450-850 nm) for determining the geographical provenance of *Eucalyptus globulus*. The experimental results demonstrate that the proposed Transformer architecture can effectively outperform traditional chemometric baselines, achieving a test accuracy and F1-score of 97.5% under a rigorous split protocol, thus validating this approach as a robust, rapid screening sensing, and cost-effective pipeline.

Provenance classification is fundamentally a kinetic physico-chemical recognition task. Our results indicate that classical methods (XGBoost and SVM) suffer from generalization constraints because they rely on static statistical compression, effectively discarding the kinetic evolution of combustion dynamics. In contrast, by modeling the full combustion kinetic cycle, the Transformer captures nonlinear spectro-kinetic

patterns. Interpretability analysis via SHAP further confirmed that the model relies on atomic emission lines, specifically the potassium emission doublet, validating the physico-chemical basis of the learned representations.

These findings validate an end-to-end deep learning framework that infers timber provenance from flame emission spectroscopy dynamics, overcoming the key limitations of traditional chemometrics. This approach enables cost-effective optical screening as a complementary method to isotopic, chemical, and genetic analyses. These findings support the development of a optical sensor for provenance verification, enhancing supply chain transparency and combating illegal timber trade.

References

[1] Dormontt, E.E., Boner, M., Braun, B., Breulmann, G., Degen, B., Espinoza, E., Gardner, S., Guillery, P., Hermanson, J.C., Koch, G., Lee, S.L., Kanashiro, M., Rimbawanto, A., Thomas, D., Wiedenhoeft, A.C., Yin, Y., Zahnen, J., Lowe, A.J.: Forensic timber identification: It's time to integrate disciplines to combat illegal logging. Biological Conservation **191**, 790–798 (2015) https://doi.org/10.1016/j.biocon.2015.06.038

[2] Ghazanfari, A., Malzl, L., Pramreiter, M., Konnerth, J., Kromoser, B.: A systematic review of strand-based engineered wood products for construction: standard test methods and mechanical properties. Wood Material Science & Engineering, 1–23 (2025)

[3] Hasan, K.F., Rahman, M.M., Rima, F.K., Sultana, J., Taher, M.A., Horváth, P.G., Garab, J., Bejó, L., Alpár, T.: Sustainable prospects of lignocellulosic wood and natural fiber-based materials in 3d and 4d printing. Advanced Composites and Hybrid Materials **8**(2), 189 (2025)

[4] Fauziyyah, S., Pipiska, T., Stojic, S., Wimmer, R.: Wood-based panels derived from fast growing tropical lightwood species: panel properties and environmental impact assessment. Wood Material Science & Engineering, 1–15 (2025)

[5] Thompson, S.T., Magrath, W.B.: Preventing illegal logging. Forest Policy and Economics **128**, 102479 (2021) https://doi.org/10.1016/j.forpol.2021.102479

[6] Gutierrez-Velez, V.H., MacDicken, K.: Quantifying the direct social and governmental costs of illegal logging in the bolivian, brazilian, and peruvian amazon. Forest Policy and Economics **10**(4), 248–256 (2008) https://doi.org/10.1016/j.forpol.2007.10.007

[7] Ipinza Carmona, R.: Resolución del conflicto en el sector forestal chileno: Una propuesta desde la teoría de juegos – abordando resultados para una solución sostenible. Ciencia & Investigación Forestal **31**(2), 93–111 (2025) https://doi.org/10.52904/0718-4646.2025.632

[8] Datta, D., Simeone, J.C., Meadows, A., Outhwaite, W., Keong Chen, H., Self,

N., Walker, L., Ramakrishnan, N.: Combating trade in illegal wood and forest products with machine learning. PloS one **20**(1), 0311982 (2025)

[9] Pumijumnong, N., Muangsong, C., Buajan, S., Songtrirat, P., Chatwatthana, R., Chareonwong, U.: Factors affecting cambial growth periodicity and wood formation in tropical forest trees: A review. Forests **14**(5), 1025 (2023)

[10] Low, M.C., Schmitz, N., Boeschoten, L.E., Cabezas, J.A., Cramm, M., Haag, V., Koch, G., Meyer-Sand, B.R.V., Paredes-Villanueva, K., Price, E., Thornhill, A.H., Brusselen, J.V., Zuidema, P.A., Deklerck, V., Dormontt, E.E., Shapcott, A., Lowe, A.J.: Tracing the worldas timber: The status of scientific verification technologies for species and origin identification. Brill Academic Publishers (2022). https://doi.org/10.1163/22941932-bja10097

[11] Štulc, A.I., Poszwa, A., Ponton, S., Dupouey, J.-L., Bouchez, J., Beuret, M., Rigoussen, D., Paul, T., Lemoine, M., Coubray, S., *et al.*: Tracing the origin of wood at the regional scale with dendrochemical markers: elemental and strontium and neodymium isotopic composition. Science of the Total Environment **957**, 177640 (2024)

[12] Jansson, D., Wolterink, A., Bergwerff, L., Hough, P., Geukens, K., Åstot, C.: Source attribution profiling of five species of amanita mushrooms from four european countries by high resolution liquid chromatography-mass spectrometry combined with multivariate statistical analysis and dna-barcoding. Talanta **186**, 636–644 (2018)

[13] Deklerck, V., Lancaster, C.A., Van Acker, J., Espinoza, E.O., Bulcke, J., Beeckman, H.: Chemical fingerprinting of wood sampled along a pith-to-bark gradient for individual comparison and provenance identification. Forests **11**(1), 107 (2020)

[14] Ravindran, P., Wiedenhoeft, A.C.: Comparison of two forensic wood identification technologies for ten meliaceae woods: computer vision versus mass spectrometry. Wood Science and Technology **54**(5), 1139–1150 (2020)

[15] Mortier, T., Truszkowski, J., Norman, M., Boner, M., Buliga, B., Chater, C., Jennings, H., Saunders, J., Sibley, R., Antonelli, A., *et al.*: A framework for tracing timber following the ukraine invasion. Nature Plants **10**(3), 390–401 (2024)

[16] Boeschoten, L.E., Rocha Venancio Meyer-Sand, B., Boom, A., Bouka, G.U.D., Ciliane-Madikou, J.C., Engone Obiang, N.L., Guieshon-Engongoro, M., Groot, A., Loumeto, J.J., Mbika, D.-m.M., *et al.*: Combined genetic and chemical methods boost the precision of tracing illegal timber in central africa. Communications Earth & Environment **6**(1), 789 (2025)

[17] Zheng, C., He, T., Jiao, L., Lu, Y., Liu, S., Li, T., Miao, Y., Feng, D., Lin, J., Feng, X., *et al.*: Deep learning-based species identification of gymnosperm xylem:

The practice in digital forestry. Computers and Electronics in Agriculture **237**, 110581 (2025)

[18] Traoré, M., Kaal, J., Cortizas, A.M.: Variation of wood color and chemical composition in the stem cross-section of oak (quercus spp.) trees, with special attention to the sapwood-heartwood transition zone. Spectrochimica Acta Part A: Molecular and Biomolecular Spectroscopy **285**, 121893 (2023)

[19] Wu, F., Gazo, R., Haviarova, E., Benes, B.: Wood identification based on longitudinal section images by using deep learning. Wood Science and Technology **55**(2), 553–563 (2021)

[20] Li, Y., Via, B.K., Young, T., Li, Y.: Visible-Near Infrared Spectroscopy and Chemometric Methods for Wood Density Prediction and Origin/Species Identification. Forests **10**(12) (2019) https://doi.org/10.3390/F10121078

[21] Chen, J., Liu, S., Yin, L., Cao, H., Xi, G., Zhang, Z., Liu, J., Luo, R., Han, L., Yin, Y., *et al.*: Non-destructive preservation state estimation of waterlogged archaeological wooden artifacts. Spectrochimica Acta Part A: Molecular and Biomolecular Spectroscopy **285**, 121840 (2023)

[22] Liu, S., Zheng, C., He, T., Zhan, W., Gasson, P., Lu, Y., Yin, Y.: Automated species discrimination and feature visualization of closely related pterocarpus wood species using deep learning models: Comparison of four convolutional neural networks. Wood Science and Technology **59**(5), 86 (2025)

[23] Kunze, D.C.G.C., Pastore, T.C.M., Rocha, H.S., Lopes, P.V.D.A., Vieira, R.D., Coradin, V.T.R., Braga, J.W.B.: Correction of the moisture variation in wood nir spectra for species identification using epo and soft pls2-da. Microchemical Journal **171**, 106839 (2021) https://doi.org/10.1016/j.microc.2021.106839

[24] Sandak, A., Sandak, J., Negri, M.: Relationship between near-infrared (nir) spectra and the geographical provenance of timber. Wood science and technology **45**(1), 35–48 (2011)

[25] Sharma, R., Kumar, R.: Chemometric analysis of UV–visible spectral data for the differentiation of Dalbergia latifolia and Dalbergia sissoo woods. Chemometrics and Intelligent Laboratory Systems **264**, 105448 (2025) https://doi.org/10.1016/j.chemolab.2025.105448

[26] Li, Y., Via, B.K., Li, Y.: Lifting wavelet transform for vis-nir spectral data optimization to predict wood density. Spectrochimica Acta Part A: Molecular and Biomolecular Spectroscopy **240**, 118566 (2020)

[27] Castillo, F., Arias, L., Cifuentes, J.: Biomass flame spectroscopy technique to identify wood species through spectral emission during combustion processes. Measurement: Journal of the International Measurement Confederation **240**

(2025) https://doi.org/10.1016/j.measurement.2024.115581

[28] Carrasco, G., Almeida, A.C., Falvey, M., Olmedo, G.F., Taylor, P., Santibañez, F., Coops, N.C.: Effects of climate change on forest plantation productivity in Chile. Global Change Biology **28**(24), 7391–7409 (2022) https://doi.org/10.1111/gcb.16418

[29] Nadeem, M., Faheem, M., Manzoor, M., Gulzar, A., Bilal, M., Jamil, Y.: Machine learning assisted libs classification of burnt and unburnt paper samples: A forensic perspective. Talanta **293**, 128073 (2025)

[30] Oñate Mardones, C.A., Arias Parada, L.E., Castillo Rivera, F.A.: Spectral analisys of the na and k traces in wood burning. In: 2023 IEEE CHILEAN Conference on Electrical, Electronics Engineering, Information and Communication Technologies (CHILECON), pp. 1–6 (2023). https://doi.org/10.1109/CHILECON60335.2023.10418640

[31] Zhong, Y., Zhang, T., Zhang, Y., Cheng, T.: Flame temperature and heat release rate sensor for active combustion control. Measurement **202**, 111762 (2022) https://doi.org/10.1016/j.measurement.2022.111762

[32] Li, K., Yan, W., Huang, X., Yu, L., Chen, Y., Lou, C.: In-situ measurement of temperature and potassium concentration during the combustion of biomass pellets based on the emission spectrum. Fuel **289**, 119863 (2021) https://doi.org/10.1016/j.fuel.2020.119863

[33] Zheng, S., Cai, W., Zhao, C., Li, D., Zhang, J., Lu, Q.: On the measurement of flame temperature and emissivity based on multispectral imaging technique. Measurement **196**, 111272 (2022) https://doi.org/10.1016/j.measurement.2022.111272

[34] Castillo, F., Arias, L., Garcés, H.O.: Estimation of temperature, local and global radiation of flames, using retrieved hyperspectral imaging. Measurement **208**, 112459 (2023) https://doi.org/10.1016/j.measurement.2023.112459

[35] Arias, L., Torres, S., Sbarbaro, D., Ngendakumana, P.: On the spectral bands measurements for combustion monitoring. Combustion and Flame **158**(3), 423–433 (2011) https://doi.org/10.1016/j.combustflame.2010.09.018

[36] Mekaoui, S., Zibordi, G.: Cosine error for a class of hyperspectral irradiance sensors. Metrologia **50**(3), 187 (2013) https://doi.org/10.1088/0026-1394/50/3/187

[37] Zhao, B., Zhang, K., Yu, Y., Yu, K., Liu, Y.: An improved method for accurate radiation measurement based on dark output noise drift compensation. Sensors **23**(13) (2023) https://doi.org/10.3390/s23136157

[38] Elissetche, J.P., Alzamora, R.M., Espinoza, Y., Emhart, V., Pincheira, M., Medina, A., Rubilar, R.: Wood basic density assessment of eucalyptus genotypes growing under contrasting water availability conditions. Forests **15**(1) (2024) https://doi.org/10.3390/f15010185

[39] Zhang, L., Luo, Z., Du, W., Li, G., Shen, G., Cheng, H., Tao, S.: Light absorption properties and absorption emission factors for indoor biomass burning. Environmental Pollution **267**, 115652 (2020)

[40] ISO, E.: 18134-3: 2015; solid biofuels—determination of moisture content—oven dry method—part 3: Moisture in general analysis sample. Polish Committee for Standardization: Warsaw, Poland (2015)

[41] Vaswani, A., Shazeer, N., Parmar, N., Uszkoreit, J., Jones, L., Gomez, A.N., Kaiser, Ł., Polosukhin, I.: Attention is all you need. Advances in neural information processing systems **30** (2017)

[42] Hendrycks, D.: Gaussian error linear units (gelus). arXiv preprint arXiv:1606.08415 (2016)

[43] Loshchilov, I., Hutter, F.: Decoupled weight decay regularization. arXiv preprint arXiv:1711.05101 (2017)

[44] Lundberg, S.M., Lee, S.-I.: A unified approach to interpreting model predictions. In: Advances in Neural Information Processing Systems, vol. 30, pp. 4765–4774 (2017)

[45] Yu, M., Yan, J., Chu, J., Qi, H., Xu, P., Wang, J., Zhou, L., Gao, J.: Accurate prediction of cross-species wood density by fusing terahertz time-domain spectroscopy and explainable machine learning. Spectrochimica Acta Part A: Molecular and Biomolecular Spectroscopy, 127348 (2025)